

Bulgeless galaxies in the COSMOS field: environment and star formation evolution at $z < 1$

Marco Grossi^{1,2*}, Cristina A. C. Fernandes^{1,3}, David Sobral^{4,5}, José Afonso^{3,6},
Eduardo Telles¹, Luca Bizzocchi⁷, Ana Paulino-Afonso^{3,6}, Israel Matute^{3,6}

¹*Observatório Nacional, Rua General José Cristino, 77, 20921-400 Rio de Janeiro, RJ, Brazil*

²*Observatório do Valongo, Universidade Federal do Rio de Janeiro, Ladeira Pedro Antônio 43, 20080-090 Rio de Janeiro, RJ, Brazil*

³*Instituto de Astrofísica e Ciências do Espaço, Universidade de Lisboa, OAL, Tapada da Ajuda, PT1349-018 Lisbon, Portugal*

⁴*Department of Physics, Lancaster University, Lancaster LA1 4YB, UK*

⁵*Leiden Observatory, Leiden University, P.O. Box 9513, NL-2300 RA Leiden, the Netherlands*

⁶*Departamento de Física, Faculdade de Ciências, Universidade de Lisboa, Edifício C8, Campo Grande, PT1749-016 Lisbon, Portugal*

⁷*Max Planck Institute for Extraterrestrial Physics, Giessenbachstrasse 1, 85748, Garching, Germany*

ABSTRACT

Combining the catalogue of galaxy morphologies in the COSMOS field and the sample of H α emitters at redshifts $z = 0.4$ and $z = 0.84$ of the HiZELS survey, we selected ~ 220 star-forming bulgeless systems (Sérsic index $n \leq 1.5$) at both epochs. We present their star formation properties and we investigate their contribution to the star formation rate function (SFRF) and global star formation rate density (SFRD) at $z < 1$. For comparison, we also analyse H α emitters with more structurally evolved morphologies that we split into two classes according to their Sérsic index n : intermediate ($1.5 < n \leq 3$) and bulge-dominated ($n > 3$). At both redshifts the SFRF is dominated by the contribution of bulgeless galaxies and we show that they account for more than 60% of the cosmic SFRD at $z < 1$. The decrease of the SFRD with redshift is common to the three morphological types but it is stronger for bulge-dominated systems. Star-forming bulgeless systems are mostly located in regions of low to intermediate galaxy densities ($\Sigma \sim 1 - 4 \text{ Mpc}^{-2}$) typical of field-like and filament-like environments and their specific star formation rates (sSFRs) do not appear to vary strongly with local galaxy density. Only few bulgeless galaxies in our sample have high (sSFR $> 10^{-9} \text{ yr}^{-1}$) and these are mainly low-mass systems. Above $M_* \sim 10^{10} \text{ M}_\odot$ bulgeless are evolving at a “normal” rate ($10^{-9} \text{ yr}^{-1} < \text{sSFR} < 10^{-10} \text{ yr}^{-1}$) and in the absence of an external trigger (i.e. mergers/strong interactions) they might not be able to develop a central classical bulge.

Key words: galaxies: evolution, galaxies: star formation, galaxies: structure, galaxies: bulges, galaxies: luminosity function, mass function.

1 INTRODUCTION

Morphologically, galaxies can be classified according to the relative importance of their two stellar components: the central spheroidal concentration known as the bulge, and the disc. Theoretical models predict that bulges form through mergers of galaxies of comparable masses (Barnes 1988; Hernquist 1992). Numerical simulations show that mergers of massive gas-rich discs disrupt the progenitors’ structure and form a central spheroidal stellar component (Barnes & Hernquist 1992; Burkert & Naab 2003). Large gas fractions can be efficiently funneled into the central regions of the merger remnants triggering a starburst

which will contribute to the formation of a “classical bulge” (Mihos & Hernquist 1996; Barnes & Hernquist 1996). On the other hand, in the absence of major merger events, no significant bulge is formed, resulting in a disc-dominated or bulgeless galaxy (e.g. Fontanot et al. 2011). This class also comprises stellar discs with a central component which looks like a bulge but has a light profile and kinematics typical of a disc, i.e. a pseudo-bulge (Kormendy & Kennicutt 2004).

Bulgeless systems are expected to evolve through time in a slow and steady process, called secular evolution, driven by the presence of stellar bars and/or spiral arms (Kormendy & Kennicutt 2004). However, the formation and survival of pure-disc galaxies within the Λ Cold Dark Matter (Λ CDM) scenario poses a challenge to theoretical mod-

* E-mail: grossi@astro.ufrj.br

els: how can stellar systems with no signs of merger-built bulges be explained by the hierarchical galaxy assembly (Barazza et al. 2008; Kormendy et al. 2010)? Recently it has been shown that discs can survive or rapidly regrow in a merger, provided that the gas fraction of the progenitors is high (Robertson et al. 2006; Robertson & Bullock 2008; Bullock et al. 2009; Font et al. 2017). Keselman & Nusser (2012) and Hammer et al. (2014) claim that pseudo bulges or even bulgeless galaxies can be formed after very gas-rich mergers. According to Governato et al. (2010) and Brook et al. (2011), a solution is provided by the presence of strong outflows from the central starburst which can remove dark and luminous matter with low angular momentum preventing the formation of a bulge. Integral field unit observations of star forming galaxies at intermediate redshifts ($z \sim 1$) showed that the angular momentum distribution is indeed a fundamental driver in defining the morphology of a galaxy and the prominence of the bulge relative to the disc (Harrison et al. 2017; Swinbank et al. 2017).

To better understand the role of bulgeless galaxies within the current picture of galaxy formation and evolution, Bizzocchi et al. (2014, hereafter B14) assembled a catalogue of such systems in the redshift range $0.4 \leq z \leq 1$ combining four of the largest and deepest multi-wavelength surveys: the Cosmological Evolutionary Survey (COSMOS; Capak et al. 2007; Scoville et al. 2007), the All-wavelength Extended Groth Strip International Survey (AEGIS; Davis et al. 2007), the Galaxy Evolution from Morphology and SEDs (GEMS) survey (Caldwell et al. 2008), and the Great Observatories Origins Deep Survey (GOODS; Giavalisco et al. 2004). The catalogue provides a first complete census of bulgeless at intermediate redshift as well as a comparison sample of more structurally evolved galaxies (from early-type spirals to lenticulars and ellipticals). Analysis of the evolution of the number density of the different morphological types with redshift showed a decrease of bulgeless with time compared to the bulge-dominated/early-type systems. This was interpreted as the evidence that internal bulge growth through either star-formation activity or mergers, and/or interactions with nearby companions can transform disc-dominated systems into earlier type morphologies through time.

The morphological transformation of disc-dominated systems into bulge-dominated ones can be driven by high density environments (Dressler 1980; Dressler et al. 1997; Baldry et al. 2006; Lackner & Gunn 2013). Indeed one of the most fundamental correlations between the properties of galaxies in the local Universe is the so-called morphology-density relation. Since the early work of Dressler (1980), a plethora of studies utilising multi-wavelength tracers of activity have shown that early-type, quiescent galaxies are preferentially found in denser environments and such a correlation is observed out to $z \sim 1$ (Kauffmann et al. 2004; van der Wel et al. 2007; Tasca et al. 2009; Scoville et al. 2013; Darvish et al. 2016). Bulgeless galaxies in the local Universe are observed in all environments, although they are preferentially located in relative isolation (the field) or in moderately dense environment such as galaxy groups (Kautsch et al. 2009).

It is thus important to investigate both the star formation process of bulgeless galaxies and the environment where

they are evolving to understand the role of secular processes and/or of galaxy interactions and mergers in their evolution.

The High-redshift(Z) Emission Line Survey (HiZELS; Geach et al. 2008; Sobral et al. 2013, hereafter S13) is a narrow-band filter survey¹ to select star-forming galaxies through their H α emission at redshifts $z = 0.40, 0.84, 1.47$ and 2.23 in the COSMOS and Ultra Deep Survey (UDS) fields. S13 revealed a clear evolution of the H α luminosity function from $z = 0$ to $z = 2.23$. At $z \sim 2$ the typical H α luminosity of galaxies and the corresponding star formation rate density (SFRD) is more than 10 times higher than locally (S13). A dominance of disc-dominated systems is observed among the selected H α emitters (Sobral et al. 2009; Paulino-Afonso et al. 2017). However, how the star formation rate function (SFRF) and the star formation process depend on galaxy morphology at intermediate redshift has not been inspected yet in detail. By combining the bulgeless catalogue of B14 and the HiZELS survey of COSMOS we aim to disentangle for the first time the contribution of each morphological class to the SFRF and SFRD, analyse the star formation properties of bulgeless galaxies at $z < 1$, investigate how star formation contributes to the growth of their stellar mass, and determine in what type of environment they are evolving.

The paper is organised as follows: Section 2 describes the sample selection and the data sets used for our study. Section 3.1 presents the SFRFs and SFRDs determined for the different morphological classes. In Section 4, we discuss the star formation properties of the selected H α emitters as a function of their morphology. In Section 5 we analyse the local environment of our sample. We summarise our results and we present our conclusions in Section 6. Throughout this paper we adopt the following values for the cosmological parameters: $H_0 = 70 \text{ km s}^{-1} \text{ Mpc}^{-1}$, $\Omega_M = 0.3$ and $\Omega_\Lambda = 0.7$. Star formation rates (SFRs) and stellar masses are derived using a Chabrier (2003) initial mass function (IMF).

2 SAMPLE AND DERIVED GALAXY PROPERTIES

2.1 Sample selection

The morphological classification of the galaxy catalogue of B14 was provided by the Advanced Camera for Surveys General Catalog (ACS-GC; Griffith et al. 2012), based on the analysis of the surface brightness profiles obtained with the Advanced Camera for Surveys (ACS) on board the Hubble Space Telescope (HST; see Griffith et al. 2012, B14 for details). The galaxy morphology was determined by fitting the surface brightness profiles with a single Sérsic profile (Sérsic 1968):

$$\Sigma(r) \propto e^{-\kappa(r/r_e)^{-1/n-1}}, \quad (1)$$

where n is the Sérsic index that defines the shape of the surface brightness profile, r_e is the effective radius of the

¹ The survey was carried out using the Wide Field Camera (WF-CAM) on the United Kingdom Infrared Telescope, Suprime-Cam on the Subaru Telescope, and the HAWK-I camera on Very Large Telescope.

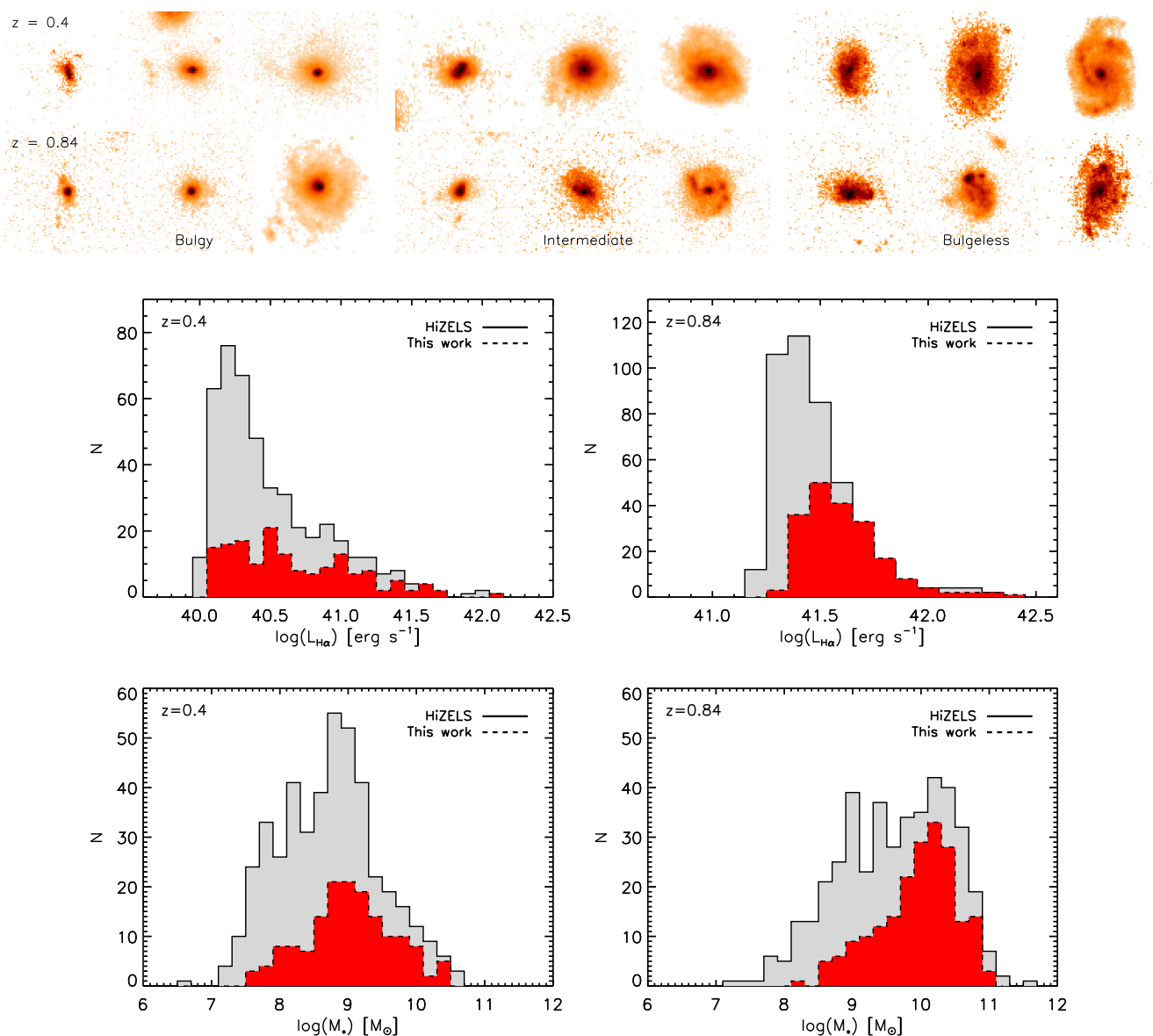


Figure 1. Top panels: HST/ACS F814W example images of galaxies selected in this work. For each morphological class (bulgy, intermediate, and bulgeless) we display galaxies with $\log M_*/M_{\odot} \approx 8.7, 9.7, 10.7$. The postage stamp size is $4'' \times 4''$. Middle panels: Comparison between the total number of sources detected in HiZELS (solid-line histograms) and the sample selected in this work (dotted-line histograms) at $z = 0.4$ (left) and $z = 0.84$ (right) as a function of the observed H α luminosity (uncorrected for dust extinction). Bottom panels: Same as middle panels but here the comparison is shown as a function of stellar masses. Because of the selection criteria adopted in the B14 catalogue, our sample includes less than 50% of the HiZELS sources detected in COSMOS.

galaxy, and κ is a parameter that is coupled to n such that half of the total flux is enclosed within r_e . A Sérsic index of $n = 1$ describes a typical pure-disc galaxy. Higher values of n correspond to galaxies with a more concentrated light distribution, with $n = 4$ giving the [de Vaucouleurs \(1959\)](#) law, generally used to describe the surface brightness profile of elliptical galaxies. In the COSMOS field fits were performed on the ACS/F814W images using the GALFIT routine ([Peng et al. 2002](#)). According to B14 bulgeless and pseudo-bulge galaxies have $n \leq 1.5$ ([Gadotti 2009](#)); disc galaxies with an increasingly prominent bulge component

are classified as intermediate galaxies if $1.5 < n \leq 3$; finally bulge-dominated, i.e. “bulgy” galaxies, have $n > 3$.

The final catalogue was then defined on the basis of the following criteria: (i) a magnitude cut of $m_{\text{AB}} \leq 24$ in the reddest filter available in the ACS surveys (F814W in COSMOS); (ii) an inclination lower than 60 deg (i.e. axial ratio $(b/a) > 0.5$), to minimise the effects of dust extinction. For each galaxy the catalogue provides rest-frame ultraviolet (UV) to near-infrared (NIR) photometry, stellar masses and morphological classification.

To investigate the star formation properties of bulgeless galaxies and their evolution through time we cross-matched

Table 1. Morphological distribution of the sample of galaxies analysed in this work. The sample is obtained by matching the H α -emitters catalogue of the HiZELS survey at $z = 0.4$ and $z = 0.84$, and the morphological catalogue of B14 in the COSMOS field.

z	Bulgeless	Intermediate	Bulgy	N_{tot}
0.40	97	39	24	160
0.84	121	39	39	199

B14 catalogue with the sample of H α emitters at $z = 0.4$ and $z = 0.84$ from the HiZELS survey (S13). HiZELS provides uniform H α coverage across UDS and COSMOS fields, covering a total area of ~ 2 deg 2 . At the two redshift bins that we consider for our study, the survey used the NB921 narrow-band filter on Suprime-Cam and the NB $_J$ filter on WFCAM. The average full width half maximum of the point spread function of the observations through these filters is 0.9 arcsec. The sample selection is carried out in two steps. First narrow-band sources are identified at each of the four redshift bins down to the same limit of H α + [N II] rest-frame equivalent width ($\text{EW}_0 = 25 \text{ \AA}$), where $\text{EW}_0 = \text{EW}_{\text{observed}}/(1+z)$. Then colour-colour diagrams ($B-R$, $i-K$), spectroscopic redshifts and high-quality photometric redshifts are used to discriminate H α emitters from possible contaminants (such as other emission lines from galaxies at different redshifts). The survey reaches an average flux limit (3σ) $S_{\text{H}\alpha+\text{[N II]}} \simeq 3$ and $7 \times 10^{-17} \text{ erg s}^{-1} \text{ cm}^{-2}$ at $z = 0.4$ and $z = 0.84$, respectively. This corresponds to a minimum H α luminosity of $1 \times 10^{40} \text{ erg s}^{-1}$ and $1.6 \times 10^{41} \text{ erg s}^{-1}$ (corrected for [N II] contamination as described in Sect. 2.2 and uncorrected for dust extinction). Because of the EW limit, the sample can be incomplete in mass, particularly at the highest masses ($> 10^{10.5} M_{\odot}$) at the lowest redshift ($z = 0.4$; S13).

We restricted the analysis to the COSMOS field for which both HiZELS observations and the morphological classification from B14 are available. The HiZELS sample in COSMOS comprises 459 H α emitters at $z = 0.4$ and 420 at $z = 0.84$ ². The B14 catalogue in the COSMOS field includes 14139 bulgeless, 7259 intermediate and 10316 bulgy galaxies at $0.4 \leq z \leq 1$. The cross-match between both catalogues with a matching radius of $1''$ resulted in a final sample of 160 and 199 galaxies at $z = 0.4$ and $z = 0.84$, respectively³. The final samples are dominated by bulgeless galaxies, which represent 60% of the total number of H α emitters (see Table 1). Example images of each morphological class at both redshifts are shown in the top panels of Fig. 1.

Because of the selection criteria adopted in B14 (mainly because of the inclination cut and the rejection of sources with bad GALFIT fits implying an unreliable morphology classification) the matched catalogue includes less than 50% of the HiZELS sources, however Fig. 1 shows that our sample

² The redshift range for which the H α line is detected over the filter bandwidths of the HiZELS survey is 0.40 ± 0.01 and 0.845 ± 0.015 (S13).

³ We inspected if increasing the matching radius would result in a larger number of sources, however up to $2''$ the number of matches increases only by $\sim 3\%$ at both redshifts.

covers the same range of observed H α luminosities (middle panels) and stellar masses (bottom panels) of the narrow-band imaging survey.

2.2 Star formation rates

The HiZELS catalogue of H α emitters (S13) provides H α fluxes which, due to the width of the narrow-band filters, can include the contribution of the adjacent [N II] lines. Thus, first we corrected the catalogue fluxes for [N II] contamination using the following relation: $\log([\text{N II}]/\text{H}\alpha) = -0.924 + 4.802 E - 8.892 E^2 + 6.701 E^3 - 2.27 E^4 + 0.279 E^5$, where $E = \log[\text{EW}_0([\text{N II}] + \text{H}\alpha)]$ (Villar et al. 2008; Sobral et al. 2012). Then we calculated the H α luminosities ($L_{\text{H}\alpha}$) assuming, similarly to S13, that the selected galaxies in each redshift bin are all at the same distance: $d = 2172$ Mpc ($z = 0.4$) and $d = 5367$ Mpc ($z = 0.845$ ⁴). We corrected $L_{\text{H}\alpha}$ by a factor of 1.14 and 1.3 at $z = 0.4$ and $z = 0.84$, respectively, to account for extended emission beyond the $3''$ and $2''$ diameter apertures used to measure the photometry (Sobral et al. 2014, hereafter S14). Lastly, we converted the H α luminosity into SFR using the standard calibration of Kennicutt (1998):

$$\text{SFR} [M_{\odot} \text{ yr}^{-1}] = 4.4 \times 10^{-42} L_{\text{H}\alpha} [\text{erg s}^{-1}] \quad (2)$$

rescaled to a Chabrier IMF (Chabrier 2003).

2.3 Stellar masses

Stellar masses were taken from S14, derived by fitting spectral energy distribution (SED) of stellar population synthesis models to the rest-frame photometry measured in 18 bands (Capak et al. 2007; Ilbert et al. 2009, 2010), ranging from far-UV (GALEX) to $8 \mu\text{m}$ (Spitzer/IRAC). The method is explained in Sobral et al. (2011) and S14 and we briefly summarise it here. The SED templates were generated with the stellar population synthesis package developed by Bruzual & Charlot (2003) using models from Bruzual (2007). The models assume a Chabrier IMF and an exponentially declining star formation history $\psi(t) = \psi_0 e^{-t/\tau}$, where ψ_0 is the SFR at the onset of the burst, t is the time since the onset of the burst, and τ the e-folding time scale assumed to vary between 0.1 and 10 Gyr. Five different metallicities were used to generate the models, from $Z = 0.0001$ to 0.05, including the solar abundance. Dust extinction was applied using the Calzetti et al. (2000) law with $E(B-V)$ in the range 0 - 0.5 (in steps of 0.05). For each source two estimates were obtained: the best-fit stellar mass, and the median M_* across all solutions in the entire multi-dimensional parameter space, lying within 1σ of the best fit. We adopted the latter values for being less sensitive to small changes in the parameter space and/or error estimations in the data set (see S14, for details). Uncertainties on the stellar masses are of the order of 0.30 dex. Similarly to the H α luminosities, stellar masses were calculated assuming that all galaxies in each redshift bin are at the same distance (see Sect. 2.2).

⁴ The corresponding volume surveyed by HiZELS in the COSMOS field is 5.1 and $10.2 \times 10^4 \text{ Mpc}^3$.

The B14 catalogue also provides stellar masses of galaxies in the COSMOS field, calculated by fitting spectral energy distribution models to galaxy photometry in the rest-frame UV, optical and near-infrared with `kcorrect` (Blanton & Roweis 2007). The main purpose of the fits is to calculate K-corrections, but the templates can also be used to derive stellar masses since they are based on the Bruzual & Charlot (2003) stellar evolution synthesis codes and they can provide an estimate of the stellar mass-to-light ratio. However, the method developed in Sobral et al. (2011) and S14 is based on a more extended set of templates and a larger number of photometric measurements and therefore we chose to use their estimates in this work.

2.4 Extinction correction: comparison between different methods

To take into account the effects of dust obscuration on the SFR derived from the $H\alpha$ emission we followed the approach of S14. We applied a correction based on the empirical relation of Garn & Best (2010) between stellar mass and dust extinction

$$A_{H\alpha}(M_*) = 0.91 + 0.77X + 0.11X^2 - 0.09X^3. \quad (3)$$

where $X = \log(M_*/10^{10}M_\odot)$. This relation was derived for a sample extracted from the Sloan Digital Sky Survey with $M_* \gtrsim 10^{8.5} M_\odot$ and it has been shown to be valid up to $z \sim 1.5$ (Sobral et al. 2012; Ibar et al. 2013)⁵. Then we calculated the intrinsic $H\alpha$ luminosity as $L_{H\alpha}^0 = L_{H\alpha}^{obs} \times 10^{0.4A_{H\alpha}}$ and used Eq. 2 to derive the intrinsic SFR, $SFR_{H\alpha}^0$. The typical uncertainty in the SFR is dominated by the uncertainty in the dust correction which corresponds to $\Delta SFR \sim 0.2$ dex (S14; Darvish et al. 2014).

In this section we investigate how the use of a different approach to treat dust attenuation would affect the SFR estimate. A robust method to derive dust-corrected SFRs consists in using a linear combination of $H\alpha$ and total infrared (TIR) luminosities, where the TIR luminosity measures the dust-obscured SFR (Calzetti et al. 2007; Kennicutt et al. 2009). L_{TIR} is usually assumed to be the luminosity between 8 and 1000 μm extrapolated from *Spitzer*/MIPS 24 μm observations (Chary & Elbaz 2001; Dale & Helou 2002). TIR luminosities were taken from the UltraVISTA catalogue (Muzzin et al. 2013), matched to our sample of $H\alpha$ emitters using a $1''$ radius and rescaled to the redshift values of $z = 0.4$ and $z = 0.845$. At $z = 0.4$ the number of galaxies detected at 24 μm is low ($\sim 32\%$), while at $z = 0.845$ most of our objects have a mid-infrared counterpart ($\sim 85\%$). The dust-corrected $H\alpha$ luminosity is given by (Kennicutt et al. 2009):

$$L_{H\alpha+TIR} = L_{H\alpha}^{obs} + 0.0024 \times L_{TIR} \quad (4)$$

⁵ We note that Eq. 3 holds until $M_* \approx M_*^{th} = 10^{8.7} M_\odot$. Below this threshold the polynomial relation starts predicting a non-physical rise of the extinction with decreasing stellar mass. Thus for galaxies with $M_* < M_*^{th}$ we applied a constant correction $A_{H\alpha}(M_*^{th}) = 0.29$ mag, corresponding to the lower end value of the range where the Garn & Best (2010) method can be applied.

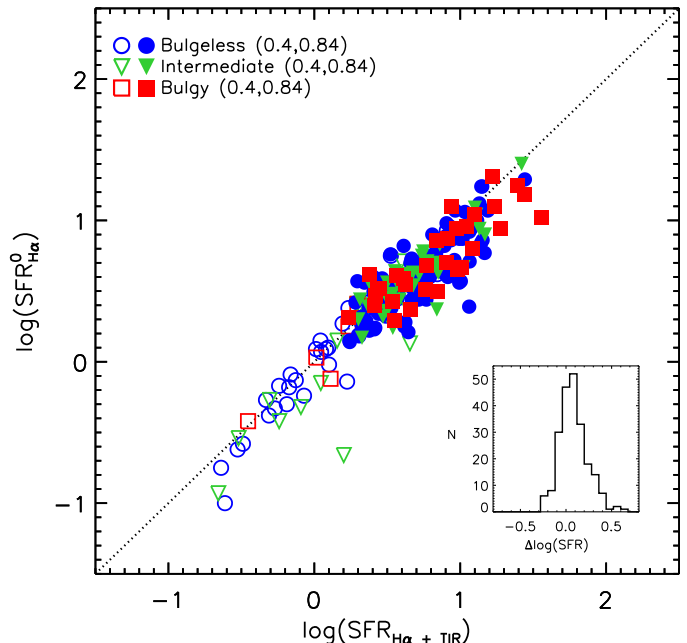


Figure 2. Comparison between the $H\alpha$ -based SFR used in this work with a mass-dependent dust extinction correction, $SFR_{H\alpha}^0$, and $SFR_{H\alpha+TIR}$ for bulgeless (circles), intermediate (upside down triangles) and bulgy galaxies (squares). Empty and filled symbols correspond to $z = 0.4$ and $z = 0.84$, respectively. The dotted lines show the one-to-one relation. The histogram of the difference between $\log(SFR_{H\alpha+TIR})$ and $\log(SFR_{H\alpha}^0)$, combining all galaxies in both redshift bins, is displayed in the box at the bottom-right corner. The mean value (and dispersion) of the difference of these two indicators is $\langle \Delta \log(SFR) \rangle = 0.06 \pm 0.13$ dex.

and the consequent SFR can then be derived from Eq. 2. Figure 2 shows the comparison between this indicator, $SFR_{H\alpha+TIR}$, and $SFR_{H\alpha}^0$. Empty and filled symbols correspond to $z = 0.4$ and $z = 0.84$, respectively. Overall, the two SFR estimates appear to be in good agreement. The mean value and the dispersion of the difference of these two indicators are $\log(SFR_{H\alpha+TIR}) - \log(SFR_{H\alpha}^0) = 0.06 \pm 0.13$ dex (combining all galaxies in both redshift bins). However, because of the lack of a MIPS detection for a large fraction of the objects in our sample (especially at $z = 0.4$), in the rest of this study we will use the intrinsic SFR derived with the extinction correction given in Eq. 3.

3 STAR FORMATION EVOLUTION WITH COSMIC TIME

3.1 SFR function

In this section we investigate the relative contribution of bulgeless, intermediate and bulgy galaxies to the SFRF, describing the number of star-forming galaxies as a function of their ongoing SFR. First we computed the number den-

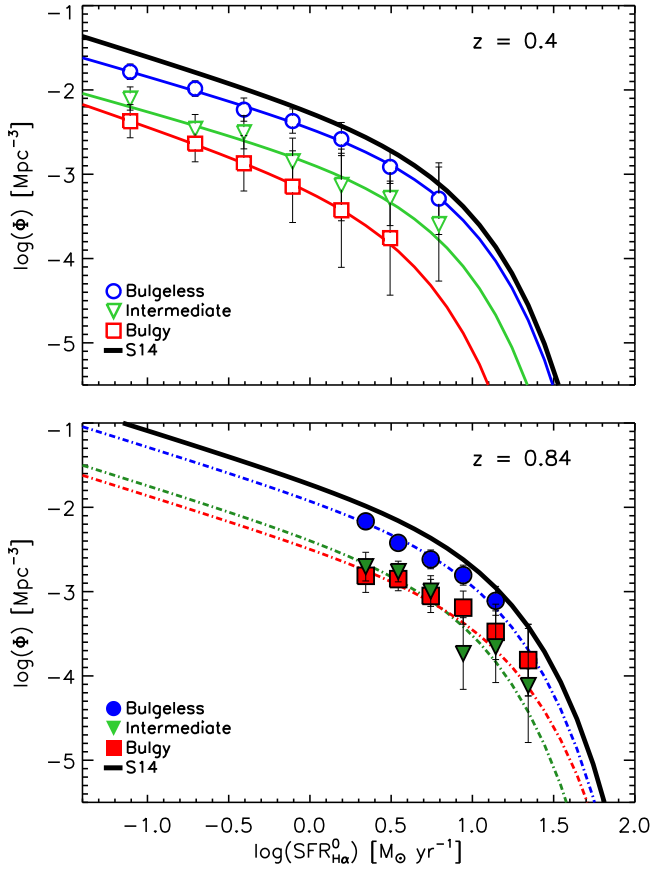


Figure 3. Best-fit SFRFs of the samples of bulgeless (circles), intermediate (upside down triangles) and bulgy galaxies (squares) at $z = 0.4$ (top panel) and $z = 0.84$ (bottom panel). The black solid lines show the SFRFs for the whole HiZELS survey at the two redshift bins taken from S14.

sity of galaxies of each morphological class (j) per bin of H α luminosity corrected for dust extinction ($L_{\text{H}\alpha}^0$):

$$\Phi_j(\log L_i) = \frac{1}{\Delta \log L} \sum_k \frac{1}{V_{\text{filter}}} \quad (5)$$

where $\log(L_i)$ is the luminosity at the centre of the bin, $\Delta \log L = 0.3$ (0.2) dex is the bin width used at $z = 0.4$ (0.84), V_{filter} is the volume probed by each narrow-band filter for the COSMOS field (5.1 and $10.2 \times 10^4 \text{ Mpc}^3$ at the lower and higher redshift, respectively), and the sum is over all galaxies with luminosity L_k within the bin of width $\Delta \log L$ centred on L_i (i.e. $|\log(\frac{L_k}{L_i})| < (\Delta \log L)/2$). To account for missing H α emitters due to the selection criteria adopted in B14, for each morphological class we applied a correction factor to $\Phi_j(\log L_i)$, $f_{\text{corr}}(\log L_i)$, that was determined as follows. Let $\Phi^{\text{T}}(\log L_i) = \sum_j \Phi_j(\log L_i)$ be the number density of galaxies of all morphologies at a given luminosity $\log L_i$. The corresponding value measured by HiZELS is $\Phi^{\text{S14}}(\log L_i)$ ⁶. We defined the correction factor as $f_{\text{corr}}(\log L_i) = \Phi^{\text{S14}}(\log L_i)/\Phi^{\text{T}}(\log L_i)$, and derive

⁶ Including completeness, volume and filter profile corrections as discussed in S13; S14.

Table 2. Best-fit parameters of the SFRFs and SFRDs of bulgeless, intermediate and bulgy galaxies at $z = 0.4$ and $z = 0.84$. Columns display the morphological class, the break of the SFRF (SFR *), normalisation density (ϕ^*), the faint-end slope (α), and the SFRD (ρ_{SFR}) obtained by integrating the SFRF over the entire luminosity range.

Morphology	$\log(\text{SFR}^*)$ [$\text{M}_{\odot} \text{ yr}^{-1}$]	$\log(\phi^*)$ [Mpc^{-3}]	α	$\log(\rho_{\text{SFR}})$ [$\text{M}_{\odot} \text{ yr}^{-1} \text{ Mpc}^{-3}$]
$z = 0.4$				
Bulgeless	0.77 ± 0.11	-3.18 ± 0.10	-1.55 ± 0.03	-2.11 ± 0.15
Intermediate	0.67 ± 0.26	-3.51 ± 0.28	-1.53 ± 0.08	-2.55 ± 0.38
Bulgy	0.51 ± 0.33	-3.78 ± 0.35	-1.66 ± 0.08	-2.86 ± 0.48
$z = 0.84$				
Bulgeless	0.98 ± 0.05	-2.83 ± 0.05	-1.6	-1.51 ± 0.07
Intermediate	0.87 ± 0.10	-3.22 ± 0.10	-1.6	-2.00 ± 0.14
Bulgy	1.04 ± 0.15	-3.44 ± 0.05	-1.6	-2.06 ± 0.16

the corrected number density per bin as $[\Phi_j(\log L_i)]_{\text{corr}} = f_{\text{corr}}(\log L_i) \Phi_j(\log L_i)$, assuming for simplicity that each morphological class is equally incomplete. Then we fitted the results with a Schechter (1976) function

$$\Phi(L) dL = \phi^* \left(\frac{L}{L^*} \right)^{\alpha} e^{-L/L^*} d \left(\frac{L}{L^*} \right) \quad (6)$$

defined by three parameters: the faint-end slope α , the luminosity of the break, L^* , and the normalisation density, ϕ^* . Lastly, we converted H α luminosities into SFR using Eq. 2 and derived the corresponding SFRFs. Results are shown in Fig. 3 for $z = 0.4$ (top panel), and $z = 0.84$ (bottom panel); the best-fit parameters and the associated 1σ errors are given in Table 2. The SFRF of bulgeless (circles), intermediate (upside down triangles) and bulgy galaxies (squares) are compared to those derived for the whole HiZELS survey (solid lines).

At $z = 0.4$ we were able to fit the three parameters simultaneously for the three SFRFs. At $z = 0.84$ the range of observed SFR is narrower ($0.2 < \log(\frac{\text{SFR}}{\text{M}_{\odot} \text{ yr}^{-1}}) < 1.5$) and our data do not sample the low-SFR end of the function preventing to constrain the faint-end slope. In this case we fixed the index α to -1.6 for the three morphologies adopting the slope from S14.

The figure shows that the galaxy number density per SFR bin is higher at earlier epochs for all morphological types. Such an evolution of the SFRF with decreasing cosmic time has been already confirmed by HiZELS out to $z = 2.2$ (S14). However, here we show that at both redshifts the SFRF is dominated by bulgeless galaxies. The number density of bulgy and intermediate H α emitters is comparable at $z = 0.84$, while at $z = 0.4$ classical bulges provide a lower contribution compared to intermediate systems. H α -luminous bulges are missing in the lower redshift bin. This could be due to the smaller volume probed at $z = 0.4$, to the increase in the number of quenched, massive bulge-dominated galaxies with decreasing redshift (Lang et al. 2014), and to the incompleteness of the survey at high stellar masses at this epoch (see Sect. 2.1).

The SFRF evolves with redshift for the three morpho-

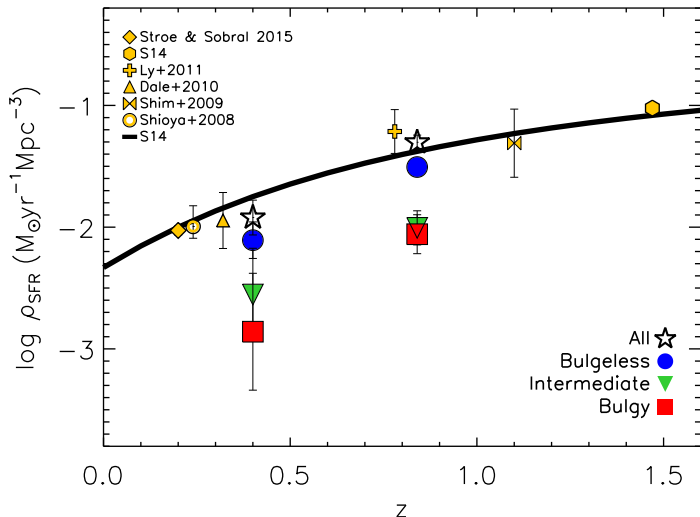


Figure 4. SFRD of the different morphological classes. Symbols are the same as in Fig. 3. The solid line represents the best fit relation of the SFRD evolution as a function of redshift for the HiZELS survey (S14). Results at lower and higher redshift taken from the literature are displayed for comparison.

logical classes. Both the break of the SFRF, SFR^* , and the normalisation density, ϕ^* increase with z . Bulgeless galaxies show a higher number density at SFR^* , while bulge-dominated galaxies show the largest variation in SFR^* , suggesting that the star formation process of these systems is more rapidly quenched between the two epochs probed (Table 2).

S14 traced the evolution of the SFRF to higher redshifts, showing that the break of the function keep increasing after $z = 0.84$ and at $z \sim 2$ it is ~ 10 times higher than at $z = 0.4$. On the other hand, ϕ^* , starts decreasing beyond $z \sim 1$, and at $z \sim 2$ it reaches roughly the same value observed at $z = 0.4$. The faint-end slope is found to scatter around $\alpha \sim -1.6$ but it remains overall constant out to $z \sim 2$.

3.2 Cosmic star formation rate density

The SFR density (SFRD) is a powerful tool to investigate the cosmic star formation history (Rowan-Robinson et al. 2016) and assessing its variation through cosmic time is a key component to describe galaxy evolution. From the present day to $z \simeq 2$, the rise of the SFRD by one order of magnitude is confirmed by several studies using different SFR tracers (Karim et al. 2011; Cucciati et al. 2012; Sobral et al. 2013; Rowan-Robinson et al. 2016). Combining the whole HiZELS sample S13 found that the rise of the SFRD with redshift can be described by $\log \rho_{SFR} \propto (1+z)^{-1}$.

With a census of star-forming galaxies of different morphological types we can determine the contribution of each class to the total SFRD (ρ_{SFR}) and trace how it evolves at $z < 1$. We estimate the SFRD by integrating the LF over the entire range of luminosities:

$$\rho_{SFR} = 4.4 \times 10^{-42} \int_0^\infty \Phi(L) L dL = \phi^* SFR^* \Gamma(\alpha + 2). \quad (7)$$

The results are displayed in Table 2 and the relative

contributions to the total SFRD of distinct galaxy populations is shown in Fig. 4.

The figure shows that bulgeless galaxies are the main contributors to the cosmic star formation history at both redshifts (65% and 62% of the total SFRD at $z = 0.4$ and $z = 0.84$, respectively), followed by intermediate (23%, 20%) and bulgy galaxies (12%, 18%). The SFRD decreases for all morphological type from $z = 0.84$ to $z = 0.4$, but the decline is faster in bulge-dominated galaxies (a factor of ~ 6) compared to bulgeless and intermediate (~ 4).

For comparison, in Fig. 4 we show results from other studies (Shioya et al. 2008; Shim et al. 2009; Dale et al. 2010; Ly et al. 2011; S14; Stroe & Sobral 2015) rescaled to a Chabrier IMF and the best-fit curve of the total SFRD found by the HiZELS survey, $\log \rho_{SFR} = -0.136T - 0.5$ (S14), where T is the age of the Universe in Gyr. The SFRD of all morphological types combined at each epoch is comparable to the trend found by the HiZELS survey and similar studies.

4 STAR FORMATION ACTIVITY OF BULGELESS GALAXIES

4.1 The main sequence of $H\alpha$ emitters

SFR and stellar mass are observed to strongly correlate in star-forming galaxies out to $z \sim 6$ (Noeske et al. 2007; Steinhardt et al. 2014; Whitaker et al. 2014; Schreiber et al. 2015). Galaxies form a distinct sequence in the SFR – M_* plane, the so-called “main sequence” (MS), with a scatter of about 0.3 dex which remains constant with z (Noeske et al. 2007; Karim et al. 2011; Whitaker et al. 2012). The evolution of the star formation activity of galaxies from the present epoch to $z \sim 2$ is characterised by a steady raise of the average SFR by a factor of ~ 20 (Madau & Dickinson 2014; Sobral et al. 2014). Star-forming galaxies on the MS formed stars at much higher rates in the past than they do today. This reflects into an evolution of the MS shifting to higher SFRs as the look-back time increases.

In Fig. 5 we show $SFR_{H\alpha}^0$ as a function of stellar mass for the three types of galaxies at $z = 0.4, 0.84$. For comparison we show the best-fit MSs obtained for the whole HiZELS sample (solid lines in the top and bottom panels of Fig. 5), that were derived selecting galaxies with masses above $10^{8.5} M_\odot$ ($z = 0.4$) and $10^9 M_\odot$ ($z = 0.84$) to avoid incompleteness issues (S14). Each relation was fit by calculating the median values in bins of 0.2 (0.1) dex at $z = 0.4$ (0.84) rather than using the individual points to avoid biases from outliers. The best-fit relation, $\log \left(\frac{SFR_{H\alpha}^0}{M_\odot \text{ yr}^{-1}} \right) = a \log \left(\frac{M_*}{M_\odot} \right) + b$, and the values of the best-fit parameters (a, b) are displayed in Fig. 5. Several studies in the literature investigated SFR – M_* relation measuring slopes within the range $a \sim 0.5 - 1.0$ (Daddi et al. 2007; Noeske et al. 2007; Santini et al. 2009; Rodighiero et al. 2011; Zahid et al. 2012; Whitaker et al. 2014). However, the derived best-fit relation at $z = 0.84$ shows a shallower slope compared to these studies. Selection effects can have a major effect on the derived MS (Speagle et al. 2014), and selection biases of the HiZELS survey may contribute to produce a shallower slope. Since the survey is flux limited, and the SFR limit at $z = 0.84$ is $\sim 1.5 M_\odot \text{ yr}^{-1}$ a large fraction of the detected galaxies at

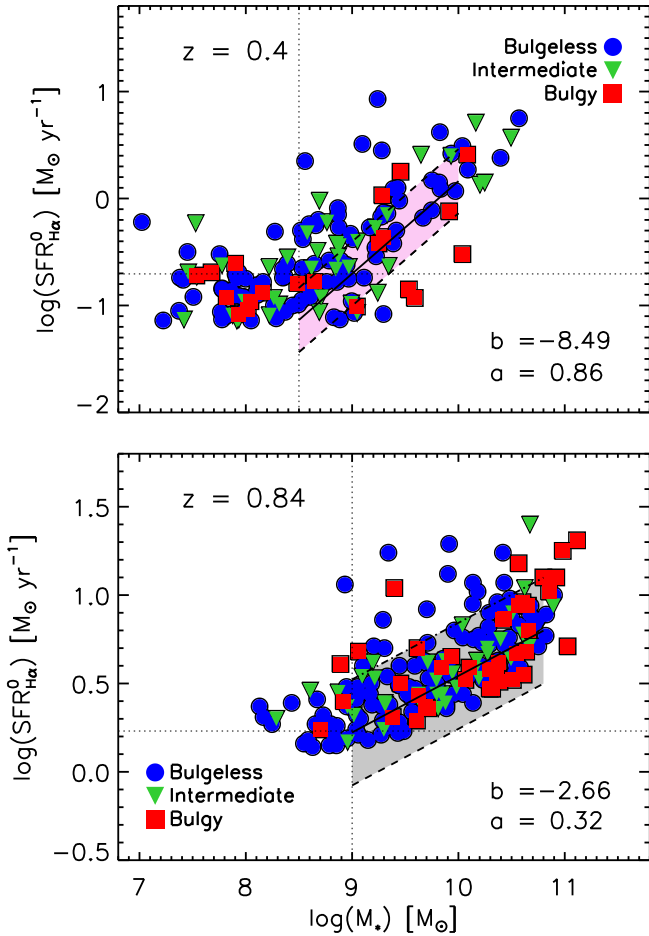


Figure 5. SFR versus stellar mass at $z=0.4$ (top panel) and $z=0.84$ (bottom panel) for bulgeless (circles), intermediate (upside down triangles) and bulgy galaxies (squares). The best-fit main sequences, $\log(\text{SFR}) = a \log(M_*) + b$, derived for the whole HiZELS sample at each redshift are overlaid for comparison (solid line), and the best-fit parameters are displayed in the bottom-right corners of each panel. The two dashed lines and the shaded areas show the typical scatter of the main sequence. Dotted lines indicate the mass and SFR completeness limits.

lower masses tend to crowd near the selection limit making the relation appear shallower (see [Darvish et al. 2014](#)).

At $z = 0.4$ the sample of H α emitters is dominated by low-mass galaxies ($\lesssim 5 \times 10^9 M_\odot$) with low SFRs ($\langle \log(\text{SFR}/M_\odot \text{ yr}^{-1}) \rangle = -0.3$). This is the consequence of the cut in EW of HiZELS which implies that at this redshift the survey is incomplete at detecting massive galaxies ($> 10^{10.5} M_\odot$; [S14](#)). Moreover the decrease in the SFRD with redshift as shown in Sect. 3.2 results in an overall lower average SFR of galaxies at $z = 0.4$ compared to $z = 0.84$. At masses below $M_* \lesssim 10^{8.5} M_\odot$ the detected galaxies tend to crowd near the the sensitivity limit of the survey ($\text{SFR} \sim 0.06 M_\odot \text{ yr}^{-1}$), defining a horizontal strip in the SFR – M_* plane ([Darvish et al. 2014](#)). Bulgeless galaxies populate the whole sequence until the more massive end, but only 17% show a SFR above $1 M_\odot \text{ yr}^{-1}$. At $z = 0.84$ the average SFR is higher by a factor of ~ 7 , $\langle \log(\text{SFR}/M_\odot \text{ yr}^{-1}) \rangle = 0.7$,

and the sample is dominated by galaxies more massive than $5 \times 10^9 M_\odot$.

As discussed in Sections 2 and 3, the sample of H α emitters is dominated by bulgeless galaxies (60% at both redshifts), implying that these systems are more actively forming stars at $z < 1$ when compared to intermediate or bulge-dominated galaxies. Only a few disc-dominated systems with $M_* > 10^9 M_\odot$ are found above the MS, suggesting an enhanced star formation activity ([Elbaz et al. 2011](#)). The majority of the sample of bulgeless systems consists in star-forming galaxies evolving along the MS, thus they are forming stars gradually over timescales that are long relative to their dynamical timescale ([Genzel et al. 2010](#); [Wuyts et al. 2011](#)).

Recently [Erfanianfar et al. \(2016\)](#) have shown a morphological dependence of the MS at high stellar masses ($> 10^{10.4} M_\odot$) at $z < 1$. Disc-dominated galaxies populate the upper envelope of the MS and tend to show a more linear relation, while bulge-dominated galaxies are located on the lower envelope of the sequence showing lower SFRs. Similarly, [Whitaker et al. \(2015\)](#) find that the presence of older bulges within star-forming galaxies contribute to decrease the slope of the MS and to its observed scatter.

At $z = 0.4$ our sample does not include enough objects with stellar masses above $10^{10} M_\odot$ to investigate trends in the MS related to galaxy morphology. At $z = 0.84$ we do not detect a flattening in the MS at high stellar masses due to the contribution of bulge-dominated galaxies, but the low-number statistics of bulgy systems at $M_* \gtrsim 10^{11} M_\odot$ prevents us from drawing robust conclusions on the role of morphology in the shape and scatter of the MS at high stellar mass. We perform the Kolmogorov-Smirnov (KS) test to compare the distribution of SFR and stellar masses among the three morphologies to assess whether they are statistically different. The values of the KS statistics and probabilities are given in Table 3. We also use the generalised two-dimensional K-S test ([Fasano & Franceschini 1987](#)) that we applied to the distribution of bulgeless, intermediate, and bulgy galaxies on the $\log(\text{SFR}_{\text{H}\alpha}^0) - \log(M_*)$ plane. We consider that the differences between distributions are significant if the estimated probability of the test, p_{KS} , is ≤ 0.05 . The test shows that at $z = 0.4$ the three distributions are statistically similar (both from the 1-D and 2-D KS tests), while at $z = 0.84$ the difference between bulgy and bulgeless galaxies is significant. Bulgy and intermediate distributions appear to be statistically different according to their stellar masses distribution. Thus the KS test yields that the MS of H α -emitting galaxies of different morphological types at $z = 0.4$ are consistent with being drawn from the same parent distribution, while at $z = 0.84$ the MS of bulgeless galaxies is more similar to intermediate rather than bulge-dominated systems. However, we caution that the difference between the distributions may not necessarily be intrinsic but it might be due to sample selection.

4.2 Evolution of specific star formation rates

One way to study the evolutionary path of galaxy populations is to analyse correlations between the specific star formation rate ($\text{sSFR} = \text{SFR}/M_*$) and parameters describing other physical properties of galaxies, such as stellar mass, Sérsic index, environment ([Elbaz et al. 2007](#);

Table 3. Results of KS test to compare the distributions of SFR and stellar masses of the different morphologies. Column 1 and 2 lists the sub-samples that are compared; column 3 and column 4 display the 1-D KS test p -values for the SFR and M_* distributions. Column 5 displays the probability of the generalised two-dimensional KS test on the distributions of the three morphological types on the SFR – M_* plane.

Sample 1	Sample 2	$p_{\text{KS}}^{\text{SFR}_{\text{H}\alpha}^0}$	$p_{\text{KS}}^{M_*}$	$p_{\text{KS}}^{\text{SFR}_{\text{H}\alpha}^0 - M_*}$
$z = 0.4$				
Bulgeless	Bulgy	0.77	0.37	0.49
Bulgeless	Intermediate	0.87	0.79	0.59
Bulgy	Intermediate	0.52	0.36	0.53
$z = 0.84$				
Bulgeless	Bulgy	0.16	0.001	0.03
Bulgeless	Intermediate	0.79	0.59	0.43
Bulgy	Intermediate	0.34	0.02	0.06

Maier et al. 2009; Whitaker et al. 2014). The inverse of the sSFR defines the time required for a galaxy to form its stellar mass at the current star formation rate, therefore this parameter is a relatively straightforward indicator of star formation activity or quiescence. The threshold sSFR to separate between actively star-forming and quiescent objects varies with studies and it ranges between 10^{-10} yr^{-1} and 10^{-11} yr^{-1} (Domínguez Sánchez et al. 2011; Bruce et al. 2012; Ibar et al. 2013; McLure et al. 2013; Domínguez Sánchez et al. 2016; Oemler et al. 2017), implying that a galaxy will double its stellar mass in a timescale $\tau = \text{sSFR}^{-1}$ comparable or greater than the age of the Universe.

The sSFR as a function of mass is shown in the left panels of Figure 6. In both redshift bins the sSFR increases as stellar mass decreases, confirming that stars are being preferentially formed in less massive systems and that star formation contributes more to the growth of low mass galaxies, as found by other studies (Cowie et al. 1996; Brinchmann et al. 2004; Bauer et al. 2005; Conroy & Wechsler 2009; Sobral et al. 2011). The drop in the global SFR from $z = 0.84$ to $z = 0.4$, as discussed in Section 4.1, is highlighted by the different distribution of the galaxies in the two panels. At $z = 0.84$ most of the galaxies lie between 1 and $10 M_{\odot} \text{ yr}^{-1}$ constant SFR line, while at $z = 0.4$ the sample is shifted to SFR values between 0.1 and $1 M_{\odot} \text{ yr}^{-1}$.

At both redshifts bulgeless galaxies span approximately 2 orders of magnitude of observed sSFR, from low-mass systems in a likely starburst phase ($\text{sSFR} \sim 10^{-8} \text{ yr}^{-1}$) to more massive ones with a normal star formation activity ($\text{sSFR} < 10^{-9} \text{ yr}^{-1}$). Massive bulgeless ($M_* > 10^{10.5} M_{\odot}$), detected mostly at $z = 0.84$, show sSFR lower than $2.5 \times 10^{-10} \text{ yr}^{-1}$, implying that their current SFR would not remarkably contribute to their stellar growth compared to the Hubble time.

On the right-hand panels of Fig. 6 we plot the sSFR versus the Sérsic index provided by the ACS-GC survey (Griffith et al. 2012). We do not find a clear separation between the star formation properties of bulges and discs. All

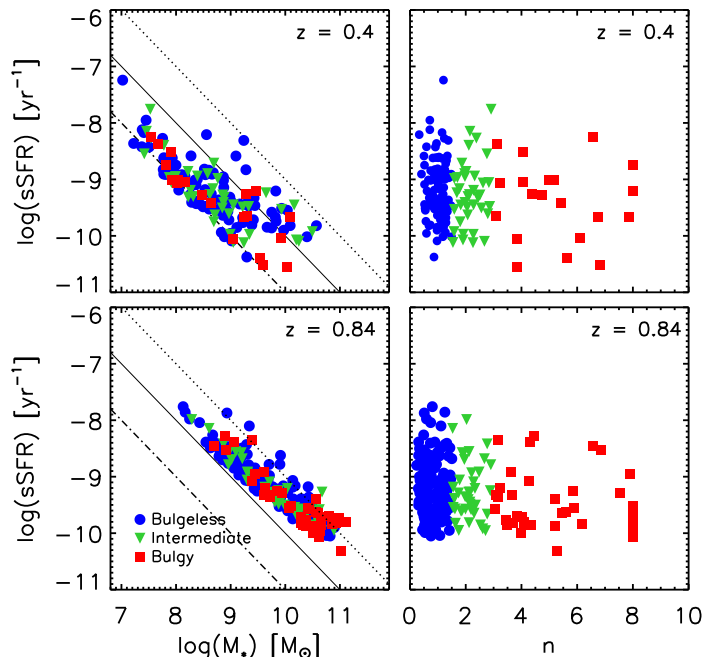


Figure 6. sSFR versus stellar mass of the different morphological classes at $z=0.4$ (top-left panel) and $z=0.84$ (bottom-left panel). Symbols are the same as in Fig. 5. Dash-dotted, solid, and dotted lines correspond to a constant SFR of 0.1, 1 and $10 M_{\odot} \text{ yr}^{-1}$. The right panels display the sSFRs versus Sérsic index n at $z=0.4$ (top-right panel) and $z=0.84$ (bottom-right panel), respectively.

the three morphological classes exhibit approximately the same range of sSFR at both redshifts, with the bulgeless extending to slightly higher values. Massive bulgy galaxies detected at $z = 0.84$ tend to occupy the region of the diagram at lower sSFRs, although a fraction of intermediate and low-mass ($M_* \sim 10^9 - 10^{10} M_{\odot}$) bulge-dominated systems show relatively high sSFRs.

Semi-analytic models expect that low luminosity/mass ellipticals may experience more extended star formation history (Khochfar & Burkert 2001). Observations in COSMOS show that intermediate-mass ($\sim 10^{10} M_{\odot}$) early-type galaxies reach into the “blue cloud” of the colour-mass diagram at $z < 1$, and that they are probably associated to low-density environments (Pannella et al. 2009). Thus at these epochs it is not uncommon to find bulge-dominated systems which are still experiencing star formation (Cassata et al. 2007; Bruce et al. 2014).

However, we note that, due to the HiZELS selection effects discussed in Sect. 2.1, at $z = 0.4$ most of the galaxies ($\sim 64\%$) have stellar masses below $10^9 M_{\odot}$. In this range, typical of dwarf galaxies, the Sérsic index classification does not provide indication about the presence or lack of a bulge because dwarf galaxies do not host a bulge. At low stellar masses our selection criteria would rather give indication about the presence of a central excess in their light distribution, usually associated to early-type dwarfs such as dwarf ellipticals (dEs), which cannot be considered as a classical bulge (Kormendy & Bender 2012)⁷. dEs can host a weak

⁷ Indeed dwarf ellipticals (dEs) can have surface brightness pro-

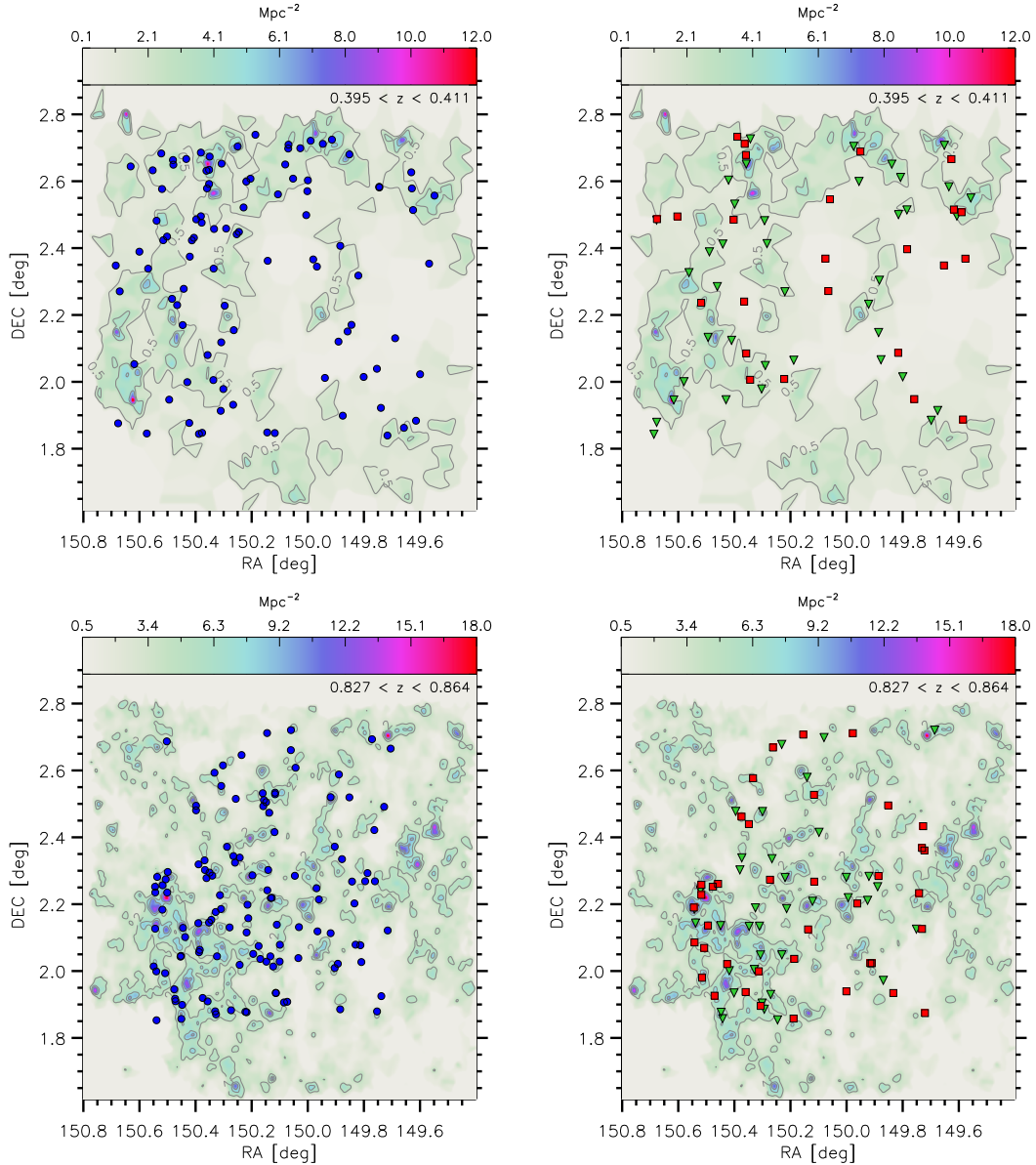


Figure 7. Spatial distribution of the bulgeless (circles), intermediate (upside down triangles), and bulgy galaxies (squares) in the COSMOS field at $0.395 < z < 0.411$ (top panels) and $0.827 < z < 0.864$ (bottom panels). Contours show the density maps of Scoville et al. (2013) at each redshift range. Densities range between 0.1 and 12 Mpc^{-2} ($z = 0.4$) and between 0.5 and 18 Mpc^{-2} ($z = 0.84$) as displayed in the colour bar on top of each panel.

star formation activity in their cores at the present day (Lisker et al. 2007; Lisker 2011) and at intermediate redshift these galaxies may still be in the process of actively forming stars before consuming their central gas distribution (Weisz et al. 2011).

files with large Sérsic indices ($n \sim 4$), but an exponential profile is also known to provide a good fit to the surface brightness profiles of these systems and the profile evolves from $n \sim 1$ to $n \sim 4$ as the total luminosity increases (Young & Currie 1994; Jerjen & Binggeli 1997; Ferrarese et al. 2006).

5 THE ENVIRONMENT OF BULGELESS GALAXIES AT $Z = 0.4$ AND $Z = 0.84$

In this section we analyse the relation between morphology, star formation activity and the local density of galaxies. As a probe of the environment we used the COSMOS density maps derived by Scoville et al. (2013), and the density fields recently recalculated by Darvish et al. (2017) out to $z = 1.2$. Scoville et al. (2013) derived the density maps using the Voronoi tessellation technique within 127 redshift bins from $z = 0.15$ to $z = 3$, where the bin widths correspond to the median of the photo- z uncertainty of galaxies within each redshift slice. The data are spatially binned in 600×600 pixels ($0''.2$) across the 2 degree field. Surface densities

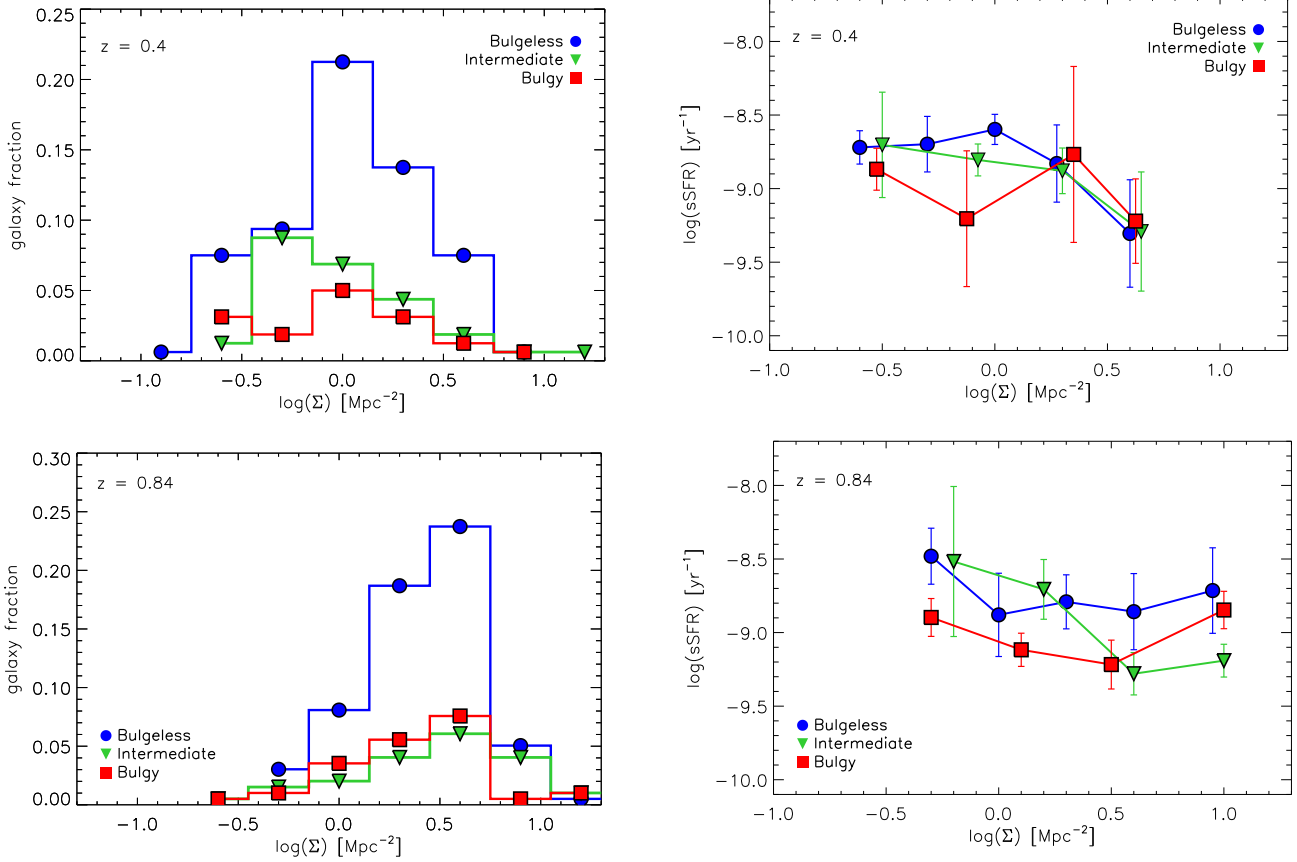


Figure 8. *Left panels:* Fraction of bulgeless (circles), intermediate (upside down triangles) and bulgy galaxies (squares) per bin of local surface density at $z = 0.4$ (top) and $z = 0.84$ (bottom). *Right panels:* Mean sSFR per bin of local surface density for the three morphological classes. Symbols are the same as the left panels. Top and bottom panels correspond to $z = 0.4$ and $z = 0.84$, respectively.

were measured from the distribution of galaxies within each redshift bin providing a map of large-scale structures out to $z = 3$ (see Scoville et al. 2013, for more details). We selected density maps in two redshift ranges $-0.395 < z < 0.411$ and $0.827 < z < 0.864$ – which fairly agree with the cosmic time interval at which the H α line is detected over the HiZELS survey filters. Darvish et al. (2017) recalculated the density field in COSMOS for a mass-complete sample of galaxies ($M_* > 10^{9.6} M_\odot$) in the redshift range $0.1 < z < 1.2$ (Laigle et al. 2016), based on the weighted adaptive kernel smoothing algorithm of Darvish et al. (2015). They separate the environment of galaxies in three main classes: field, filaments, and clusters. The authors also provide a version of the catalogue derived by interpolating all galaxies in the same redshift range to the density field, without applying any cut in mass. For our analysis at the lower redshift bin we used the version with no stellar mass cuts because of the large fraction of galaxies with $M_* < 10^{9.6} M_\odot$ selected at $z = 0.4$.

We selected all galaxies in Darvish et al. (2017) within the redshift ranges sampled by HiZELS ($0.39 < z < 0.41$ and $0.83 < z < 0.86$), we cross-matched them to our list of targets, and then we assigned to each H α emitters the local density and environment of the closest galaxy in their catalogue. Comparing the Scoville et al. (2013) and Darvish et al. (2017) methods we found that Scoville et al.

(2013) densities are underestimated on average by a factor of ~ 1.7 (1.3) at $z \sim 0.4$ ($z \sim 0.84$). However, using either of the two methods does not alter our main conclusions. In the rest of this section we will adopt the local density measurements and the environmental classes defined in Darvish et al. (2017) and the Scoville et al. (2013) maps to show the spatial distribution of our sample.

Figure 7 shows the surface density fields of galaxies in the COSMOS field for the selected redshift slices. The maps were obtained by summing the densities over the range of redshifts specified on each plot. The figures show the spatial clustering of the galaxies in COSMOS and the corresponding location of the bulgeless (circles), intermediate (upside down triangles) and bulgy galaxies (squares) in each redshift bin. At $z = 0.4$ only few structures are identified: two main filament-like structures are visible in the northern and south-eastern part of the field.

At $z = 0.84$ the selected redshift range is larger ($0.83 < z < 0.86$) and the COSMOS map shows the presence of a larger number of overdensities in the region. A ~ 10 Mpc structure is visible in the south-east side of the field. It contains X-ray confirmed clusters/groups (Finoguenov et al. 2007), and it has been interpreted as a large filament connecting overdensities in this region, characterised by an enhancement in the number of H α emitters (Sobral et al. 2011; Darvish et al. 2014). Indeed, the bottom panels of Fig. 7

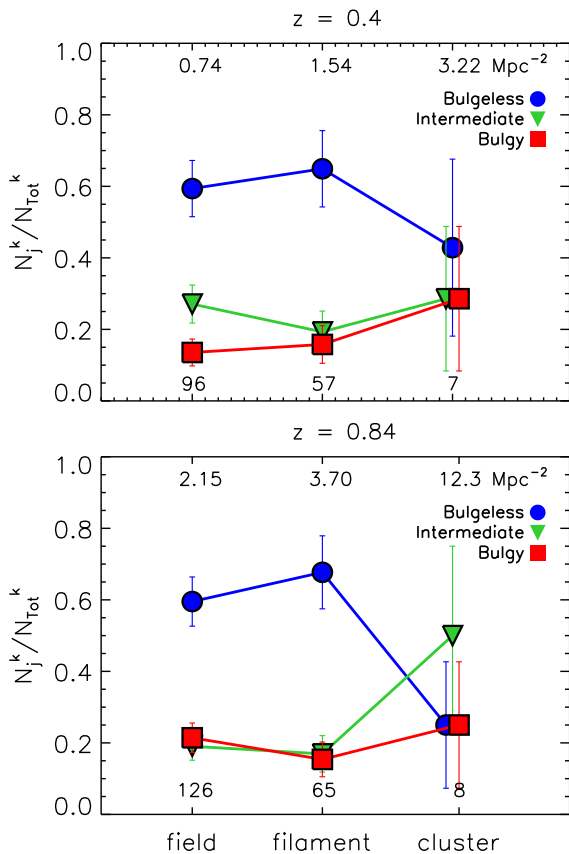


Figure 9. *Left panels:* Ratio of number of bulgeless (circles), intermediate (upside down triangles) and bulgy galaxies (squares) to the total number of galaxies found in different cosmic environments at $z = 0.4$ (top) and $z = 0.84$ (bottom). The index j represents the morphological type and the index k the environmental class in the y -axis label. The total number of galaxies in each type of environment (N_{Tot}^k) and the median density in each environmental class are shown at the bottom and at the top of each panel, respectively. Error bars are evaluated assuming Poisson statistics.

show a higher concentration of galaxies of all morphologies in this region.

In Fig. 8 we display the galaxy fraction, i.e. the ratio of the number of galaxies of each morphological class (j) per bin of surface density Σ_i to total, N_i^j/N_{Tot} , as a function of environmental density. At $z = 0.4$ (top-left panel), galaxies are found in very similar environments (i.e. mostly at low galaxy surface densities) independent of morphologies. The peak of the three distributions occurs approximately at the same value, $\Sigma \sim 1 \text{ Mpc}^{-2}$, and only $\sim 10\%$ of all bulgeless are found in environments with densities $\Sigma > 3 \text{ Mpc}^{-2}$. According to Darvish et al. (2017) most of the galaxies at this redshift are found in field-like environments (top-panel of Fig. 9). At $z = 0.84$ (bottom-left panel) the peak of the bulgeless galaxies distribution occurs at $\log(\Sigma/\text{Mpc}^{-2}) = 0.6$, corresponding to environments classified as “rich field” or filament-like (Darvish et al. 2014, 2017). About 10% of the bulgeless are found at densities higher than $\Sigma \gtrsim 6 \text{ Mpc}^{-2}$.

Subsequently, we analyse whether there is a correlation between the star formation activity, traced by the sSFR pa-

rameter, and the density of the local environment. Again we compare the two epochs and we show the results in the right panels of Fig. 8, where we display the mean sSFR of galaxies per density bin for the three morphological classes. Vertical error bars correspond to the 1σ distribution of the sSFR in each density bin. At $z = 0.84$ the sSFR stays roughly constant through the range of surface densities that we are inspecting and we do not find a clear trend between sSFR and Σ for all morphologies⁸, in agreement with the analysis of Darvish et al. (2014) based on the same data set. At $z = 0.4$ the sSFR of bulgeless and intermediate galaxies show hints of a moderate decrease at higher densities, however given the large dispersion in these bins it is difficult to draw strong conclusions about morphology-density trends at this redshift. Erfanianfar et al. (2016) observed a decline of SFR in galaxies in groups in the redshift range $0.1 < z < 0.5$, while at higher redshift ($0.5 < z < 1.1$) no variation in the SFR is found when comparing galaxies in the field or in groups, suggesting that environmental processes responsible for the suppression of the star formation activity only appear at lower redshifts.

Lastly, using the environment classes defined by Darvish et al. (2017) we show in Fig. 9 the distribution of the different morphological types in clusters, filaments and the field⁹. For each environmental class, k , we calculate the total number of H α emitters (N_{Tot}^k), and the fraction of bulgeless, intermediate, and bulgy galaxies N_j^k/N_{Tot}^k . The total number of H α emitters in each environment is displayed in the lower part of the panels, and the median density in each environmental class is shown in the upper part. H α emitters of all morphologies are mostly found in field-like and filament-like environments at these redshifts, and very few are located in cluster/rich groups. The fraction of bulgeless, intermediate and bulgy does not remarkably vary in the field and filaments environments at both redshifts. Bulgeless constitute about 60% of the total number of H α emitters while the fraction of intermediate and bulgy is similar ($\sim 20\%$). The figure shows hints of a potential decline in the fraction of bulgeless in cluster environments. However, the number of galaxies found in this bin at both redshifts is too small to draw conclusions about morphological segregation trends at higher densities.

6 SUMMARY AND CONCLUSIONS

Combining the catalogue of B14 in the COSMOS field and the catalogue of H α -selected star-forming galaxies from the HiZELS survey (S13), we assembled a sample of H α -emitting galaxies in the redshift bins $z = 0.4$ and $z = 0.84$ with a robust morphological classification. We split the selected targets in three classes according to their Sérsic index n : bulgeless ($n \leq 1.5$), intermediate ($1.5 < n \leq 3$) and bulge-dominated ($n > 3$). We studied the dependence of the SFRF,

⁸ However, we note that despite the large dispersion, a potential slight decrease of the sSFR can be identified for intermediate galaxies at higher densities.

⁹ We caution that, as mentioned in Darvish et al. (2017) there is substantial overlap between the densities obtained for the galaxies in different environments, which implies that a pure density-based criterion is not fully adequate to identify cosmic web structures.

of the SFRD and of the MS on the morphology of galaxies and expand the scope of previous studies based on these data sets. Particularly, we investigated the star formation properties of bulgeless galaxies and explored their star formation evolution with cosmic time.

We showed that bulgeless galaxies contribute significantly more than intermediate and bulgy galaxies to the SFRF both at $z = 0.4$ and $z = 0.84$, and that they are the dominant contributors to the SFRD at $z < 1$. We confirmed the decrease of the SFRD of galaxies from $z = 0.84$ to $z = 0.4$ as reported by other studies, but here we showed that such a decline is common to all morphological types experiencing star formation and it is faster for bulge-dominated systems compared to intermediate and bulgeless morphologies.

Analysis of the sSFR versus stellar mass plots at $z = 0.4$ and $z = 0.84$ support the scenario where more massive star-forming galaxies evolve at a lower rate at recent epochs (Bundy et al. 2007), while lower mass galaxies are still actively forming stars. We do not find a clear separation between the star formation properties of bulges and discs, and the three classes span a similar range of sSFR independently of morphology. Our sample of H α emitters includes a number of low-mass high Sérsic index galaxies with significant ongoing star formation activity.

Using local surface density measurements in the COSMOS field by Darvish et al. (2017) we investigated the local environment of our sample. At both redshifts bulgeless galaxies (and in general the whole sample of H α emitters) are mostly located in regions of low and intermediate density typical of field-like and filament-like environments. The star formation activity of the different morphologies as traced by the sSFR does not change with local surface density, suggesting that environment is not driving the evolution of our targets. However, the number of objects detected at high local surface densities is too small to draw conclusions about the interplay between high-density environments and morphology in our sample.

Only few disc-dominated systems have high sSFRs ($> 10^{-9} \text{ yr}^{-1}$) and these have mainly low stellar masses. Above $M_* \sim 10^{10} M_\odot$ bulgeless are evolving at a “normal” rate ($10^{-9} \text{ yr}^{-1} < \text{sSFR} < 10^{-10} \text{ yr}^{-1}$). Internal evolution (or secular) processes in discs such as bars can funnel gas into the centre but they are expected to lead to the formation of non classical or pseudo-bulges (Kormendy & Kennicutt 2004; Kormendy 2013; Sellwood 2014). Simulations show that a pure disc galaxy evolving from $z = 1$ to present with a gradually decreasing SFR (from 2 to $1 M_\odot \text{ yr}^{-1}$) without going through a major merging phase will form a long-lived bar by $z \sim 0.4$ and it will develop a pseudo-bulge by $z = 0$ (Brook et al. 2012). At the present epoch this galaxy will look like a Sbc/d type with a stellar mass of $1.4 \times 10^{10} M_\odot$. Results from the Eris simulation succeed in reproducing a slightly more massive late-type spiral galaxy with a pseudo-bulge ($M_* = 4 \times 10^{10} M_\odot$ at $z = 0$) assuming a quiet late merger history (last minor merger at $z = 1$) and a secular evolution at redshift lower than 1 (Guedes et al. 2011). This seems to suggest that given the observed sSFRs and in the absence of an external trigger (mergers/strong interactions) our sample of more massive bulgeless galaxies ($M_* \gtrsim 10^{10} M_\odot$) might not be able to build a central classical bulge.

ACKNOWLEDGEMENTS

We thank the anonymous referee for the constructive and timely comments that helped us improve the manuscript. M.G. gratefully acknowledges support from CNPq through grant 152120/2016-5 associated with the program CSF - CONCF. C.A.C.F. gratefully acknowledges support from CNPq (through PCI-DA grant 302388/2013-3 associated with the PCI/MCT/ON program) and past financial support from the Foundation for Science and Technology (FCT Portugal) through project grant PTDC/FIS/100170/2008. D.S. acknowledges financial support from the Netherlands Organisation for Scientific research (NWO) through a Veni fellowship. J.A., I.M., and A.P.A. acknowledge financial support from the Science and Technology Foundation (FCT, Portugal) through research grants PTDC/FIS-AST/2194/2012, UID/FIS/04434/2013 and fellowships SFRH/BPD/95578/2013 (I.M.), PD/BD/52706/2014 (A.P.A.). This project has been completed as part of the project “A Bulgeless side of Galaxy Evolution” financed by the Portuguese Science and Technology Foundation (FCT, Portugal) through grant PTDC/CTE-AST/105287/2008.

REFERENCES

- Baldry I. K., Balogh M. L., Bower R. G., Glazebrook K., Nichol R. C., Bamford S. P., Budavari T., 2006, *MNRAS*, **373**, 469
- Barazza F. D., Jooe S., Marinova I., 2008, *ApJ*, **675**, 1194
- Barnes J., 1988, in *Bulletin of the American Astronomical Society*. p. 733
- Barnes J. E., Hernquist L., 1992, *ARA&A*, **30**, 705
- Barnes J. E., Hernquist L., 1996, *ApJ*, **471**, 115
- Bauer A. E., Drory N., Hill G. J., Feulner G., 2005, *ApJ*, **621**, L89
- Bizzocchi L., et al., 2014, *ApJ*, **782**, 22
- Blanton M. R., Roweis S., 2007, *AJ*, **133**, 734
- Brinchmann J., Charlot S., White S. D. M., Tremonti C., Kauffmann G., Heckman T., Brinkmann J., 2004, *MNRAS*, **351**, 1151
- Brook C. B., et al., 2011, *MNRAS*, **415**, 1051
- Brook C. B., Stinson G., Gibson B. K., Roškar R., Wadsley J., Quinn T., 2012, *MNRAS*, **419**, 771
- Bruce V. A., et al., 2012, *MNRAS*, **427**, 1666
- Bruce V. A., et al., 2014, *MNRAS*, **444**, 1001
- Bruzual G., 2007, in Vallenari A., Tantaló R., Portinari L., Moretti A., eds, *Astronomical Society of the Pacific Conference Series Vol. 374, From Stars to Galaxies: Building the Pieces to Build Up the Universe*. p. 303 ([arXiv:astro-ph/0702091](https://arxiv.org/abs/astro-ph/0702091))
- Bruzual G., Charlot S., 2003, *MNRAS*, **344**, 1000
- Bullock J. S., Stewart K. R., Purcell C. W., 2009, in Andersen J., Nordström B., Bland-Hawthorn J., eds, *IAU Symposium Vol. 254, The Galaxy Disk in Cosmological Context*. pp 85–94 ([arXiv:0811.0861](https://arxiv.org/abs/0811.0861)), [doi:10.1017/S1743921308027427](https://doi.org/10.1017/S1743921308027427)
- Bundy K., Treu T., Ellis R. S., 2007, *ApJ*, **665**, L5
- Burkert A., Naab T., 2003, in Contopoulos G., Voglis N., eds, *Lecture Notes in Physics, Berlin Springer Verlag Vol. 626, Galaxies and Chaos*. pp 327–339 ([arXiv:astro-ph/0301385](https://arxiv.org/abs/astro-ph/0301385)), [doi:10.1007/978-3-540-45040-5_27](https://doi.org/10.1007/978-3-540-45040-5_27)
- Caldwell J. A. R., et al., 2008, *ApJS*, **174**, 136
- Calzetti D., Armus L., Bohlin R. C., Kinney A. L., Koornneef J., Storchi-Bergmann T., 2000, *ApJ*, **533**, 682
- Calzetti D., et al., 2007, *ApJ*, **666**, 870
- Capak P., et al., 2007, *ApJS*, **172**, 99
- Cassata P., et al., 2007, *ApJS*, **172**, 270
- Chabrier G., 2003, *PASP*, **115**, 763

- Chary R., Elbaz D., 2001, *ApJ*, **556**, 562
- Conroy C., Wechsler R. H., 2009, *ApJ*, **696**, 620
- Cowie L. L., Songaila A., Hu E. M., Cohen J. G., 1996, *AJ*, **112**, 839
- Cucciati O., et al., 2012, *A&A*, **539**, A31
- Daddi E., et al., 2007, *ApJ*, **670**, 156
- Dale D. A., Helou G., 2002, *ApJ*, **576**, 159
- Dale D. A., et al., 2010, *ApJ*, **712**, L189
- Darvish B., Sobral D., Mobasher B., Scoville N. Z., Best P., Sales L. V., Smail I., 2014, *ApJ*, **796**, 51
- Darvish B., Mobasher B., Sobral D., Scoville N., Aragon-Calvo M., 2015, *ApJ*, **805**, 121
- Darvish B., Mobasher B., Sobral D., Rettura A., Scoville N., Faisst A., Capak P., 2016, *ApJ*, **825**, 113
- Darvish B., Mobasher B., Martin D. C., Sobral D., Scoville N., Stroe A., Hemmati S., Kartaltepe J., 2017, *ApJ*, **837**, 16
- Davis M., et al., 2007, *ApJ*, **660**, L1
- Domínguez Sánchez H., et al., 2011, *MNRAS*, **417**, 900
- Domínguez Sánchez H., et al., 2016, *MNRAS*, **457**, 3743
- Dressler A., 1980, *ApJ*, **236**, 351
- Dressler A., et al., 1997, *ApJ*, **490**, 577
- Elbaz D., et al., 2007, *A&A*, **468**, 33
- Elbaz D., et al., 2011, *A&A*, **533**, A119
- Erfanianfar G., et al., 2016, *MNRAS*, **455**, 2839
- Fasano G., Franceschini A., 1987, *MNRAS*, **225**, 155
- Ferrarese L., et al., 2006, *ApJS*, **164**, 334
- Finoguenov A., et al., 2007, *ApJS*, **172**, 182
- Font A. S., McCarthy I. G., Le Brun A. M. C., Crain R. A., Kelvin L. S., 2017, preprint, ([arXiv:1710.00415](https://arxiv.org/abs/1710.00415))
- Fontanot F., De Lucia G., Wilman D., Monaco P., 2011, *MNRAS*, **416**, 409
- Gadotti D. A., 2009, *MNRAS*, **393**, 1531
- Garn T., Best P. N., 2010, *MNRAS*, **409**, 421
- Geach J. E., Smail I., Best P. N., Kurk J., Casali M., Ivison R. J., Coppin K., 2008, *MNRAS*, **388**, 1473
- Genzel R., et al., 2010, *MNRAS*, **407**, 2091
- Giavalisco M., et al., 2004, *ApJ*, **600**, L93
- Governato F., et al., 2010, *Nature*, **463**, 203
- Griffith R. L., et al., 2012, *ApJS*, **200**, 9
- Guedes J., Callegari S., Madau P., Mayer L., 2011, *ApJ*, **742**, 76
- Hammer F., IMAGES Team 2014, Mem. Soc. Astron. Italiana, **85**, 329
- Harrison C. M., et al., 2017, *MNRAS*, **467**, 1965
- Hernquist L., 1992, *ApJ*, **400**, 460
- Ibar E., et al., 2013, *MNRAS*, **434**, 3218
- Ilbert O., et al., 2009, *ApJ*, **690**, 1236
- Ilbert O., et al., 2010, *ApJ*, **709**, 644
- Jerjen H., Binggeli B., 1997, in Arnaboldi M., Da Costa G. S., Saha P., eds, *Astronomical Society of the Pacific Conference Series* Vol. 116, *The Nature of Elliptical Galaxies*; 2nd Stromlo Symposium. p. 239 ([arXiv:astro-ph/9701221](https://arxiv.org/abs/astro-ph/9701221))
- Karim A., et al., 2011, *ApJ*, **730**, 61
- Kauffmann G., White S. D. M., Heckman T. M., Ménard B., Brinchmann J., Charlot S., Tremonti C., Brinkmann J., 2004, *MNRAS*, **353**, 713
- Kautsch S. J., Gallagher J. S., Grebel E. K., 2009, *Astronomische Nachrichten*, **330**, 1056
- Kennicutt Jr. R. C., 1998, *ARA&A*, **36**, 189
- Kennicutt Jr. R. C., et al., 2009, *ApJ*, **703**, 1672
- Keselman J. A., Nusser A., 2012, *MNRAS*, **424**, 1232
- Khochfar S., Burkert A., 2001, *ApJ*, **561**, 517
- Kormendy J., 2013, *Secular Evolution in Disk Galaxies*. p. 1
- Kormendy J., Bender R., 2012, *ApJS*, **198**, 2
- Kormendy J., Kennicutt Jr. R. C., 2004, *ARA&A*, **42**, 603
- Kormendy J., Drory N., Bender R., Cornell M. E., 2010, *ApJ*, **723**, 54
- Lackner C. N., Gunn J. E., 2013, *MNRAS*, **428**, 2141
- Laigle C., et al., 2016, *ApJS*, **224**, 24
- Lang P., et al., 2014, *ApJ*, **788**, 11
- Lisker T., 2011, in Koleva M., Prugniel P., Vauglin I., eds, *EAS Publications Series* Vol. 48, *EAS Publications Series*. pp 171–180, [doi:10.1051/eas/1148040](https://doi.org/10.1051/eas/1148040)
- Lisker T., Grebel E. K., Binggeli B., Glatt K., 2007, *ApJ*, **660**, 1186
- Ly C., Lee J. C., Dale D. A., Momcheva I., Salim S., Staudaheer S., Moore C. A., Finn R., 2011, *ApJ*, **726**, 109
- Madau P., Dickinson M., 2014, *ARA&A*, **52**, 415
- Maier C., et al., 2009, *ApJ*, **694**, 1099
- McLure R. J., et al., 2013, *MNRAS*, **428**, 1088
- Mihos J. C., Hernquist L., 1996, *ApJ*, **464**, 641
- Muzzin A., et al., 2013, *ApJS*, **206**, 8
- Noeske K. G., et al., 2007, *ApJ*, **660**, L43
- Oemler Jr. A., Abramson L. E., Gladders M. D., Dressler A., Poggianti B. M., Vulcani B., 2017, *ApJ*, **844**, 45
- Pannella M., et al., 2009, *ApJ*, **701**, 787
- Paulino-Afonso A., Sobral D., Buitrago F., Afonso J., 2017, *MNRAS*, **465**, 2717
- Peng C. Y., Ho L. C., Impey C. D., Rix H.-W., 2002, *AJ*, **124**, 266
- Robertson B. E., Bullock J. S., 2008, *ApJ*, **685**, L27
- Robertson B., Bullock J. S., Cox T. J., Di Matteo T., Hernquist L., Springel V., Yoshida N., 2006, *ApJ*, **645**, 986
- Rodighiero G., et al., 2011, *ApJ*, **739**, L40
- Rowan-Robinson M., et al., 2016, *MNRAS*, **461**, 1100
- Santini P., et al., 2009, *A&A*, **504**, 751
- Schechter P., 1976, *ApJ*, **203**, 297
- Schreiber C., et al., 2015, *A&A*, **575**, A74
- Scoville N., et al., 2007, *ApJS*, **172**, 1
- Scoville N., et al., 2013, *ApJS*, **206**, 3
- Sellwood J. A., 2014, *Reviews of Modern Physics*, **86**, 1
- Sersic J. L., 1968, *Atlas de galaxias australes*
- Shim H., Colbert J., Teplitz H., Henry A., Malkan M., McCarthy P., Yan L., 2009, *ApJ*, **696**, 785
- Shioya Y., et al., 2008, *ApJS*, **175**, 128
- Sobral D., et al., 2009, *MNRAS*, **398**, 75
- Sobral D., Best P. N., Smail I., Geach J. E., Cirasuolo M., Garn T., Dalton G. B., 2011, *MNRAS*, **411**, 675
- Sobral D., Best P. N., Matsuda Y., Smail I., Geach J. E., Cirasuolo M., 2012, *MNRAS*, **420**, 1926
- Sobral D., Smail I., Best P. N., Geach J. E., Matsuda Y., Stott J. P., Cirasuolo M., Kurk J., 2013, *MNRAS*, **428**, 1128
- Sobral D., Best P. N., Smail I., Mobasher B., Stott J., Nisbet D., 2014, *MNRAS*, **437**, 3516
- Speagle J. S., Steinhardt C. L., Capak P. L., Silverman J. D., 2014, *ApJS*, **214**, 15
- Steinhardt C. L., et al., 2014, *ApJ*, **791**, L25
- Stroe A., Sobral D., 2015, *MNRAS*, **453**, 242
- Swinbank A. M., et al., 2017, *MNRAS*, **467**, 3140
- Tasca L. A. M., et al., 2009, *A&A*, **503**, 379
- Villar V., Gallego J., Pérez-González P. G., Pascual S., Noeske K., Koo D. C., Barro G., Zamorano J., 2008, *ApJ*, **677**, 169
- Weisz D. R., et al., 2011, *ApJ*, **739**, 5
- Whitaker K. E., van Dokkum P. G., Brammer G., Franx M., 2012, *ApJ*, **754**, L29
- Whitaker K. E., et al., 2014, *ApJ*, **795**, 104
- Whitaker K. E., et al., 2015, *ApJ*, **811**, L12
- Wuyts S., et al., 2011, *ApJ*, **738**, 106
- Young C. K., Currie M. J., 1994, *MNRAS*, **268**, L11
- Zahid H. J., Dima G. I., Kewley L. J., Erb D. K., Davé R., 2012, *ApJ*, **757**, 54
- de Vaucouleurs G., 1959, *Handbuch der Physik*, **53**, 311
- van der Wel A., et al., 2007, *ApJ*, **670**, 206